International Journal of Mechanical and Sustainability Engineering Technology

Journal homepage: https://uniexpertsacademy.com/index.php/IJMSET/index
ISSN: 3083-8363



Optimization of Two-Step Rectangular Rib Geometries for Enhanced Thermal Performance in Interrupted Microchannels

Nadwan Majeed Ali[1,*]

[1] Al-Furat-Al-Awsat Technical University, Al-Musayyab Technical Institute, Babylon, Iraq.

ARTICLE INFO

Article history:
Received 13 August 2026
Received in revised form 16 September 2026
Accepted 16 September 2026
Available online 17 September 2026

Keywords:

Microchannel heat sink, 2-step rectangular rib, rib optimization, thermal performance, grid independence, numerical simulation, heat transfer enhancement.

ABSTRACT

As microelectronic devices continue to increase in power density, efficient thermal management becomes increasingly critical. Traditional microchannel heat sinks often struggle to meet the cooling demands of high-performance systems. This work investigates multi-step rectangular ribs (step count N∈{2,3,4}) in interrupted MCHS and optimizes the two-step topology. ANSYS Fluent was used to simulate the flow and heat transfer characteristics, with grid independence tests confirming the optimal mesh size. The analysis reveals that rib geometry, including multi-step and two-step rib configurations, significantly influences heat transfer and pressure drop, with optimal configurations identified for different operating conditions. The results demonstrate that optimized rib dimensions enhance heat transfer efficiency while managing pressure losses, with the performance evaluated in terms of Nusselt number, friction factor, and thermal enhancement factor across varying Reynolds numbers. This work provides valuable insights for the design of advanced microchannel heat sinks in high-performance electronic applications.

1. Introduction

The continuous increase in power density and functional integration of microelectronic devices has made thermal management a major limitation in the design of high-performance electronic systems [1]. As heat generation becomes more localized within compact chips and electronic modules, conventional cooling approaches are often unable to remove high heat fluxes effectively without increasing the size and complexity of the cooling system. Microchannel heat sinks have therefore attracted considerable attention because they provide a large surface-area-to-volume ratio, short heat-conduction paths, and high convective heat-transfer capability within a compact geometry [2,3]. Since the pioneering work of Tuckerman and Pease on liquid-cooled microchannels for VLSI applications, microchannel heat sinks have been widely investigated as promising candidates for cooling microprocessors, power electronics, MEMS devices, and other compact high-heat-flux systems [2,3]. However, despite their high thermal potential, their practical

* *Corresponding author.*
E-mail address: nadwan.ali.ims@atu.edu.iq

performance is strongly constrained by the need to enhance heat transfer while avoiding excessive pressure drop and pumping-power consumption [3].

Several passive enhancement strategies have been proposed to overcome the thermal limitations of straight microchannel heat sinks. Xu et al. introduced the concept of thermal boundary-layer redevelopment in microscale heat transfer and proposed interrupted microchannel arrays with transverse channels to repeatedly restart the developing thermal field [4]. This concept was later extended through three-dimensional conjugate simulations of interrupted and conventional microchannel heat sinks, where the interrupted configuration was formed by shortened parallel microchannels connected through transverse microchambers [5]. Other studies improved microchannel performance by introducing passive internal structures, including stacked two-layer microchannels with MEMS-compatible mixing structures [6], offset strip-fin microchannel networks [7], and longitudinal internal fins, where fin geometry was shown to influence both heat-transfer enhancement and pressure loss [8]. Further developments used sidewall or reentrant cavities to increase surface area, disturb the boundary layer, and generate jetting, throttling, or recirculating flow structures; examples include offset fan-shaped cavities [9], aligned fan-shaped cavities [10], triangular reentrant cavities [11], periodic expansion–constriction cross-sections [12], and fan-shaped cavities combined with internal ribs [13,14].

More recent studies also examined sinusoidal cavities with rectangular ribs and different rib geometries as methods for improving the thermo-hydraulic performance of microchannel heat sinks [15,16]. Among these works, the study by Chai et al. is the closest benchmark to the present paper because it specifically investigated interrupted microchannel heat sinks with rectangular ribs placed in transverse microchambers and optimized the rib width, rib length, rib-row position, and microchamber spacing using Nusselt number, friction factor, and thermal enhancement factor [17]. However, that work considered conventional single-level rectangular ribs, whereas the present study extends the same interrupted-MCHS concept by examining multi-step rectangular ribs and then optimizing the two-step rib topology.

Despite these advances, the geometric development of rectangular ribs in interrupted microchannel heat sinks has mainly been limited to conventional single-level ribs or simple rib-shape variations. In particular, the closest previous study optimized the size and position of rectangular ribs in transverse microchambers but did not examine whether a rib divided into multiple stepped levels could provide a better balance between flow mixing, boundary-layer interruption, and pressure-loss penalty [17]. Therefore, the present study extends the interrupted-MCHS concept by introducing multi-step rectangular ribs with step numbers N=2,3, and 4, and then focuses on the detailed optimization of the two-step topology. The influence of the upper-step area ratio A_2/A is evaluated over Re=300"-" 700 using three-dimensional CFD simulations in ANSYS Fluent. The performance is assessed in terms of the average Nusselt number, friction factor, pressure drop, and thermal enhancement factor at equal pumping power. In this way, the study aims to identify a rib geometry that improves heat-transfer performance while maintaining an acceptable hydraulic penalty.

2. Numerical Methodology

A three-dimensional numerical study was carried out to investigate the thermo-hydraulic performance of interrupted microchannel heat sinks equipped with multi-step rectangular ribs. The configuration consists of longitudinal microchannels periodically interrupted by transverse microchambers, in which rectangular rib structures are placed to disturb the developing boundary layer and promote secondary flow mixing. Following the unit-cell modeling approach commonly used for interrupted microchannel heat sinks, only one representative microchannel and its surrounding

solid substrate were simulated in order to reduce computational cost while preserving the main conjugate heat-transfer behaviour of the complete heat sink [3,4]. The present work was performed in two stages. First, the influence of rib step number was examined by comparing multi-step rectangular ribs with N=2, 3, and 4. Second, based on the observed performance of the multi-step configurations, the two-step rectangular rib was selected for detailed geometric optimization. The optimization parameter was the upper-step area ratio, A_2/A, where A denotes the base rib area and A_2 denotes the projected area of the upper step. All cases were evaluated over the Reynolds-number range Re=300"-" 700.

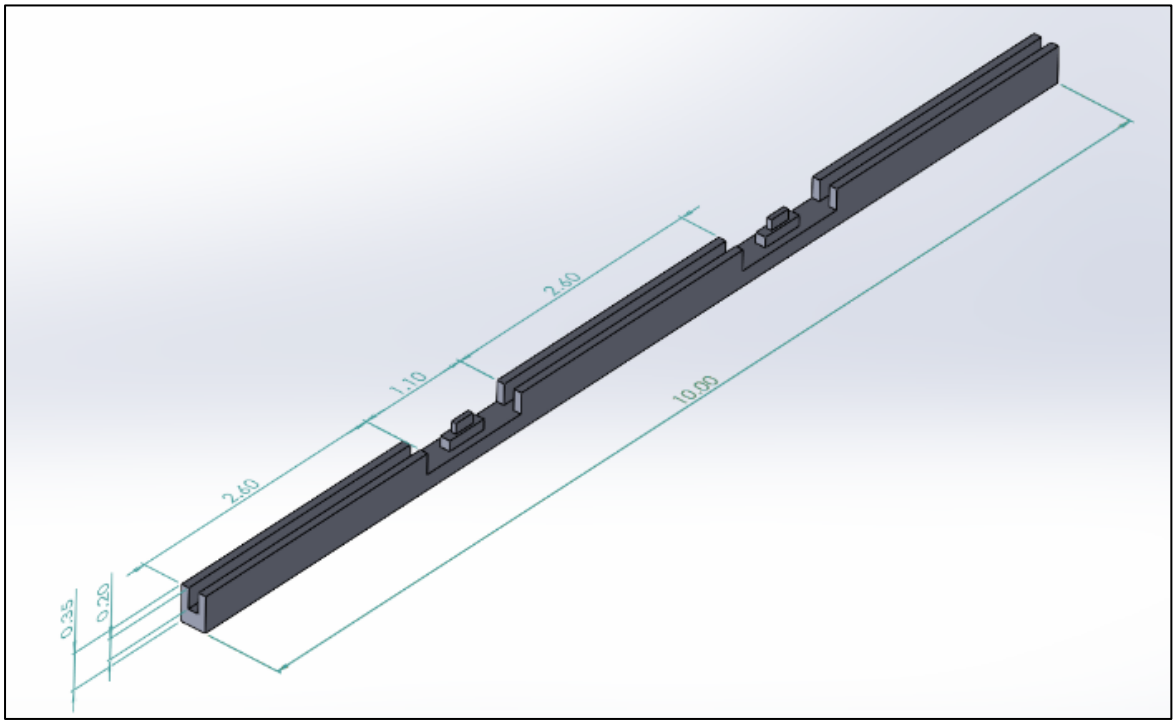


Fig. 1. Computational unit cell of the interrupted microchannel heat sink with two-step rectangular ribs in the transverse microchambers.

The baseline geometry is an interrupted microchannel heat sink with transverse microchambers and rectangular ribs. The streamwise length of the computational unit cell is $L = 10\ \mathrm{mm}$. The representative transverse microchamber length is $1.10\ \mathrm{mm}$, the straight-run segment is $2.80\ \mathrm{mm}$, and the channel depth is $0.35\ \mathrm{mm}$. The rib geometry is defined by the number of stacked rectangular steps, N. For the two-step rib, the lower step has the base projected area A, while the upper step has the projected area A_2. The ratio A_2/A is used as the main geometric parameter for the two-step optimization. For a general multi-step rib, the width, length, and height of the i-th step are denoted by w_i, l_i, and h_i, respectively. The arrangement of the rib row inside the transverse microchamber is described by the rib-row position and the spacing between adjacent transverse microchambers. These definitions follow the same geometric logic used in interrupted microchannel studies and in rectangular-rib transverse-microchamber designs, but are adapted here to a stepped rectangular-rib topology [5,17].

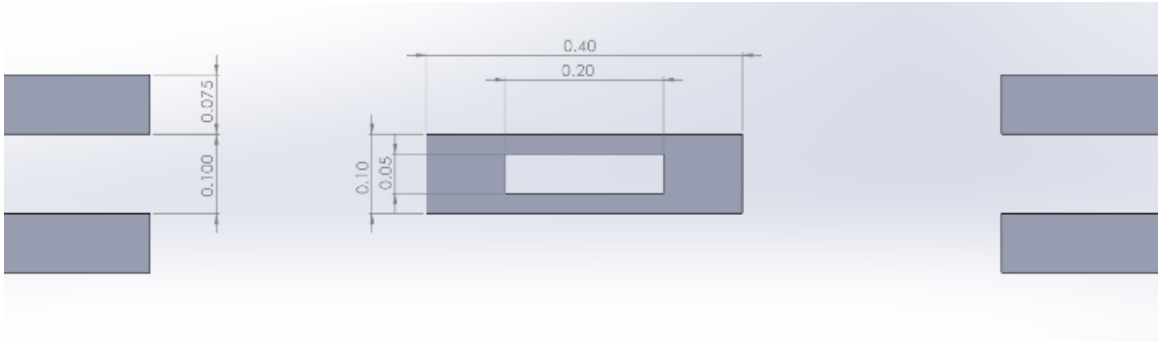


Fig. 2. Detailed dimensions and labelling of the two-step rib (Add: A, A_2, w_1, w_2, l_1, l_2, h_1, h_2, and flow direction).

Table 1. Baseline geometric dimensions of the computational model.

Parameter	Symbol	Value
Unit-cell streamwise length	L	$10\ \mathrm{mm}$
Transverse microchamber length	—	$1.10\ \mathrm{mm}$
Straight-run segment	—	$2.80\ \mathrm{mm}$
Channel depth	—	$0.35\ \mathrm{mm}$
Step number	N	$2,\ 3,\ 4$
Upper-step area ratio	A_2/A	$0.5,\ 0.75,\ 1.25,\ 1.5$
Reynolds-number range	Re	$300–700$

The flow was assumed to be steady, laminar, incompressible, and single-phase. Water was used as the working fluid, and the silicon substrate was treated as the solid heat-conduction domain. A conjugate heat-transfer model was adopted, so the fluid-flow equations and the solid heat-conduction equation were solved simultaneously. Temperature-dependent water properties were used, and viscous dissipation was retained in the fluid energy equation, consistent with established microchannel heat-transfer modeling practice [17,18,21].

The continuity equation is written as:

$$\nabla \cdot (\rho \mathbf{u}) = 0.$$

The momentum equation is

$$\rho(\mathbf{u} \cdot \nabla)\mathbf{u} = -\nabla p + \nabla \cdot [\mu(\nabla \mathbf{u} + (\nabla \mathbf{u})^T)].$$

The fluid energy equation is

$$\rho c_p(\mathbf{u} \cdot \nabla T) = \nabla \cdot (k_f \nabla T) + \Phi,$$

where Φ is the viscous-dissipation term. Heat conduction in the solid substrate is governed by

$$\nabla \cdot (k_s \nabla T) = 0.$$

Water properties $\rho(T), \mu(T), k_f(T), c_p(T)$ are listed in Table 2.

Table 2. Temperature-dependent thermophysical properties of water.

T (K)	ρ (kg·m^{-3})	cp (J·kg^{-1}·K^{-1})	k (W·m^{-1}·K^{-1})	μ (Pa·s)
293	998.2	4183	0.599	0.001004
303	995.7	4174	0.618	0.0008015
313	992.2	4174	0.635	0.0006533
323	988.1	4174	0.648	0.0005494
333	983.1	4179	0.659	0.0004699
343	977.8	4187	0.668	0.0004061
353	971.8	4195	0.674	0.0003551
363	965.3	4208	0.680	0.0003149

This setup is consistent with established practice for interrupted-MCHS computations. No-slip and no-penetration boundary conditions were imposed on all fluid–solid walls:

$$u = v = w = 0.$$

At the inlet, a uniform mean velocity was prescribed to obtain the required Reynolds numbers in the range $Re = 300–700$. At the outlet, a fixed static-pressure boundary condition was applied. The fluid inlet temperature was set to

$$T_{in} = 293 \text{ K}.$$

A uniform heat flux of

$$q'' = 1.22 \text{ MW m}^{-2}$$

was applied to the bottom surface of the silicon substrate. The outer top surface of the solid domain was treated as adiabatic, while the lateral planes of the unit cell were modeled as symmetry boundaries. At the fluid–solid interfaces, both temperature continuity and heat-flux continuity were enforced:

$$T_f = T_s,$$
$$-k_f \frac{\partial T_f}{\partial n} = -k_s \frac{\partial T_s}{\partial n}.$$

At the outlet, a zero-diffusive-flux condition was applied for temperature. These boundary conditions are consistent with the interrupted-MCHS modeling framework used in previous numerical studies [17]. The governing equations were solved using ANSYS Fluent with a pressure-

based, steady, laminar solver. The finite-volume method was used for spatial discretization, following standard CFD practice [19,22]. Second-order discretization was applied to improve numerical accuracy, and the solver setup was implemented according to the ANSYS Fluent formulation [27]. Convergence was assessed using normalized residuals and monitored flow/thermal quantities. In addition to residual reduction, the stability of the outlet velocity field, pressure drop, and heat-transfer quantities was checked to ensure that the final solution was not changing with further iterations.

An unstructured mesh with local refinement was generated for the computational domain. Strong refinement was applied in the transverse microchamber and around the stepped ribs, where large velocity and temperature gradients were expected. The mesh was also refined near the fluid–solid walls to improve the resolution of the boundary-layer region. Grid independence was examined by comparing the velocity distribution along an outlet vertical probe line at $x = 10\ \mathrm{mm}$ over $z = 0.15–0.35\ \mathrm{mm}$. Four mesh levels were considered, approximately 2×10^5, 4×10^5, 6×10^5, and 8×10^5 elements. The mesh with approximately 6×10^5 elements was selected because further refinement to approximately 8×10^5 elements produced negligible variation in the sampled velocity profile. This grid-independence procedure follows standard CFD verification practice [28,29].

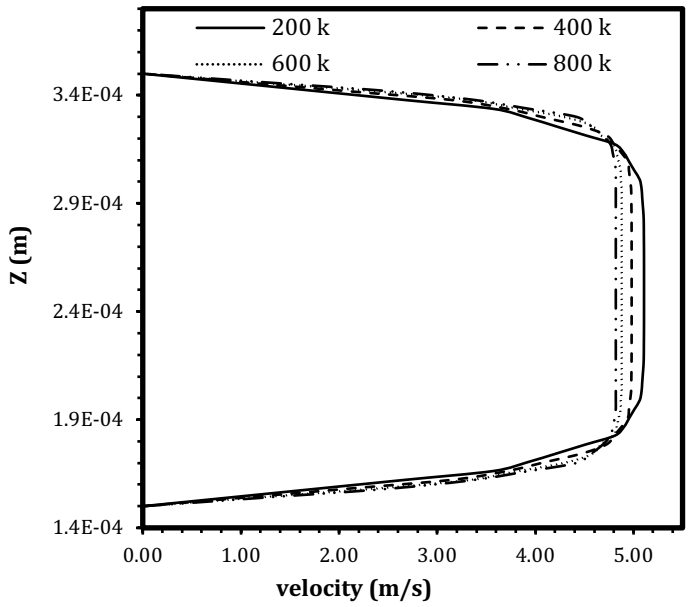


Fig. 3. Grid-independence probe: velocity along the outlet vertical line at $x = 10\ \mathrm{mm}$ for $z = 0.15–0.35\ \mathrm{mm}$.

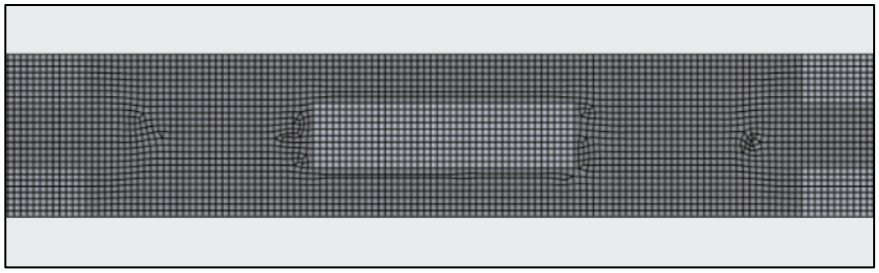


Fig. 4. Selected mesh (top view).

The performance of each configuration was evaluated using the Reynolds number, pressure drop, friction factor, average Nusselt number, and thermal enhancement factor. The Reynolds number is defined as

$$Re = \frac{\rho u_m D}{\mu},$$

where ρ is the fluid density, u_m is the mean inlet velocity, D is the hydraulic diameter, and μ is the dynamic viscosity.

The pressure drop is obtained from the difference between the area-averaged inlet and outlet static pressures:

$$\Delta p = p_{in} - p_{out}.$$

The friction factor is calculated as

$$f = \frac{2\Delta p D}{\rho L u_m^2},$$

where L is the heated length of the computational domain.

The local Nusselt number is defined as

$$Nu(x) = \frac{h(x) D}{k_f},$$

where $h(x)$ is the local convective heat-transfer coefficient and k_f is the thermal conductivity of the fluid. The bulk fluid temperature is calculated by mass-flow averaging:

$$T_b(x) = \frac{\int_A \rho u \, c_p T \, dA}{\int_A \rho u \, c_p \, dA}.$$

The average Nusselt number over the heated length is

$$\bar{Nu} = \frac{1}{L}\int_0^L Nu(x) \, dx.$$

The overall thermo-hydraulic performance was assessed using the thermal enhancement factor at equal pumping power:

$$\eta = \frac{\bar{Nu}/\bar{Nu}_0}{(f/f_0)^{1/3}},$$

where the subscript 0 denotes the straight rectangular microchannel baseline. This criterion is commonly used to evaluate whether heat-transfer enhancement is sufficient to compensate for the accompanying increase in flow resistance [3,18,19].

To validate the numerical model, the predicted average Nusselt number was compared with the published interrupted-MCHS results of Chai et al. [17]. The comparison was performed over the Reynolds-number range $Re = 300–700$. The maximum relative deviation was calculated as

$$\text{Maximum deviation} = \max_i \left| \frac{\bar{Nu}_{i,\text{present}} - \bar{Nu}_{i,\text{ref}}}{\bar{Nu}_{i,\text{ref}}} \right| \times 100\%.$$

The maximum deviation was 6.98%, indicating acceptable agreement between the present model and the reference data. Therefore, the numerical setup was considered suitable for the subsequent parametric investigation.

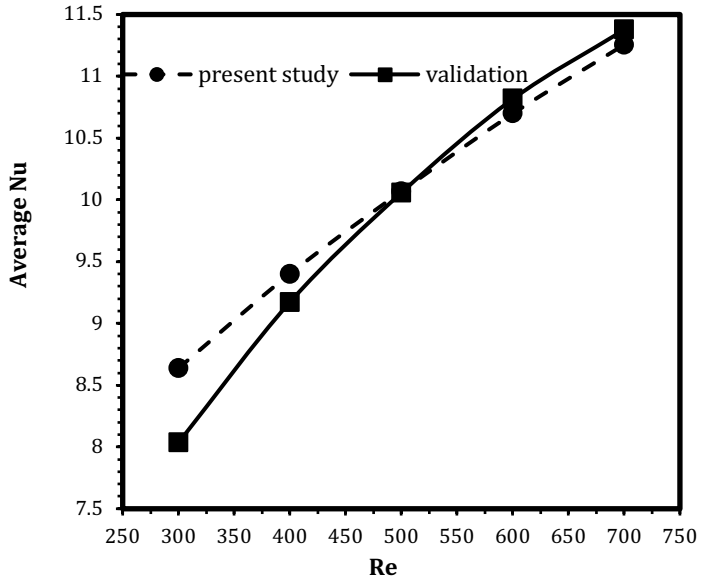


Fig. 5. Comparison of simulated average Nusselt number with Chai et al. [17].

Two parametric sweeps were performed. The first sweep examined the effect of rib step number, N, for $N = 2$, 3, and 4. The second sweep focused on the two-step configuration and examined the influence of the upper-step area ratio, A_2/A. All simulations were conducted over $Re = 300–700$.

Table 3. Parametric design matrix.

Sweep	Parameter	Levels	Reynolds-number range	Purpose
A	Step number	$N = 2,\ 3,\ 4$	300–700	To compare multi-step rib configurations
B	Upper-step area ratio	$A_2/A = 0.5,\ 0.75,\ 1.25,\ 1.5$	300–700	To optimize the two-step rib topology

3. Results and Discussion

The numerical results are discussed in terms of the thermal and hydraulic performance of the interrupted microchannel heat sink with multi-step rectangular ribs. The analysis follows two successive stages. First, the effect of rib step number is examined for N=2, 3, and 4 to identify the most effective multi-step configuration. Second, the selected two-step rib topology is further optimized by varying the upper-step area ratio, A_2/A. For all cases, the performance is evaluated using the normalized average Nusselt number, (Nu) ¯/(Nu) ¯_0, the normalized friction factor, f/f_0, and the thermal enhancement factor, η, where the subscript 0 denotes the straight rectangular microchannel baseline. This evaluation approach is consistent with previous studies on interrupted microchannel heat sinks, where heat-transfer enhancement must be considered together with the associated pressure-drop penalty [17].

3.1. Effect of step count in multi-step rectangular ribs

Figure 6 compares the heat-transfer and hydraulic performance of the interrupted microchannel heat sink with different rib step numbers, $N = 2$, 3, and 4, over the Reynolds-number range $Re = 300–700$. As shown in Fig. 6(a), all multi-step rib configurations provide higher heat-transfer performance than the straight rectangular microchannel baseline, indicating that the stepped rib structures enhance the thermal interaction between the fluid and the heated wall. This improvement can be attributed to the combined influence of boundary-layer interruption, local flow disturbance, and increased mixing inside the transverse microchamber. Similar mechanisms were reported for rectangular ribs in transverse microchambers, where ribs were shown to induce mainstream separation, recirculation, and interruption of the thermal boundary layer [17].

Among the tested configurations, the two-step rib generally gives the highest $\bar{Nu}/\bar{Nu}_0$ over most of the investigated Reynolds-number range. The three-step and four-step ribs also improve heat transfer relative to the baseline channel, but their additional step complexity does not produce a proportional increase in the average Nusselt number. This indicates that increasing the number of steps does not automatically improve the thermal performance. Although additional steps may increase local geometric complexity, they can also modify the flow passage in a way that limits the effective mixing benefit or changes the balance between recirculation and main-flow transport. The corresponding friction-factor ratios are presented in Fig. 6(b). The values of f/f_0 remain higher than unity for all ribbed configurations, confirming that the use of ribs increases the hydraulic resistance compared with the straight rectangular microchannel. This behavior is expected because rib structures obstruct the flow, generate local acceleration and deceleration regions, and introduce additional form drag inside the transverse microchamber. The differences among the three step-count cases are relatively smaller for the friction factor than for heat-transfer performance, which suggests that the hydraulic penalty is present for all stepped-rib designs and must be judged together with the heat-transfer gain. The thermal enhancement factor shown in Fig. 6(c) provides a combined evaluation of heat-transfer enhancement and frictional loss at equal pumping power. The two-step rib exhibits the best overall performance among the tested step numbers, especially at moderate and higher Reynolds numbers. This result means that the two-step geometry provides a more

favorable balance between boundary-layer disturbance and pressure-drop penalty than the three-step and four-step configurations. Therefore, the two-step rib is selected as the preferred topology for the next stage of optimization, where the influence of the upper-step area ratio A_2/A is examined in detail.

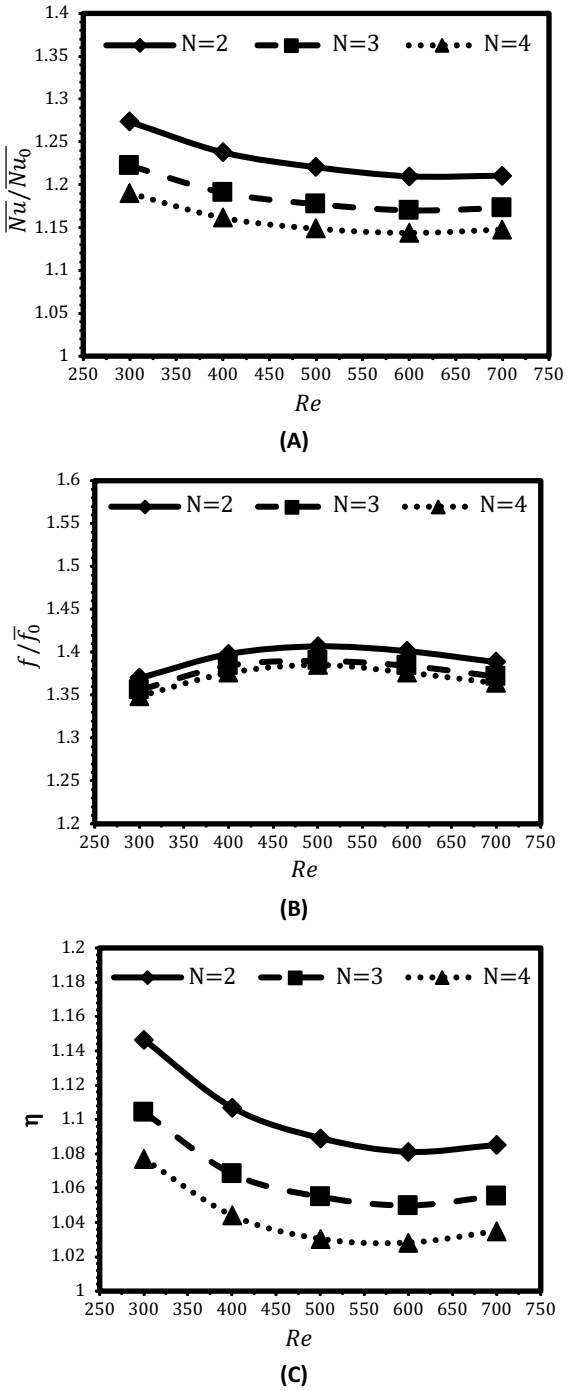


Fig. 6. (A) Variation of $\overline{\boldsymbol{Nu}}/\overline{\boldsymbol{Nu_0}}$, (B) variation of $\bar{\boldsymbol{f}}/\bar{\boldsymbol{f}}_{\boldsymbol{0}}$ and (C) variation of η with Re for different multi-step ribs.

Table 4. Variation of $\overline{Nu}/\overline{Nu}_0$ with Re for different multi-step ribs.

Channels/Re	300	400	500	600	700
2	1.3	1.54	1.52	1.51	1.50
3	1.52	1.49	1.47	1.47	1.47
4	1.49	1.46	1.44	1.44	1.44

Table 5. Variation of $\overline{f}/\overline{f}_0$ with Re for different multi-step ribs.

Channels/Re	300	400	500	600	700
2	1.57	1.6	1.61	1.6	1.59
3	1.56	1.57	1.59	1.58	1.57
4	1.55	1.56	1.58	1.56	1.56

At $Re = 300$, the three-step design gives the highest heat-transfer gain, with $\bar{N}u/\bar{N}u_0 = 1.52$, followed by the four-step design at 1.49 and the two-step design at 1.30. As the Reynolds number increases, the ranking reverses. For $Re = 400$, 500, 600, and 700, the two-step configuration gives the largest heat-transfer ratios of 1.54, 1.52, 1.51, and 1.50, respectively, while the three-step and four-step configurations remain slightly lower. The friction-factor ratios remain within a relatively narrow range for all step numbers. The two-step case gives $f/f_0 \approx 1.57$–1.61, while the three-step and four-step cases remain only marginally lower. These results indicate that $N = 3$ can be competitive at the lowest tested Reynolds number, but $N = 2$ provides the most favorable overall behavior for moderate-to-high Reynolds numbers. This justifies selecting the two-step rib for the detailed area-ratio optimization in the following section.

3.2 Two-step ribs: effect of upper-step area ratio A_2/A

After identifying the two-step rib as the preferred topology, the influence of the upper-step area ratio, A_2/A, was examined in detail. Figure 7 compares the normalized average Nusselt number, normalized friction factor, and thermal enhancement factor for $A_2/A = 0.5$, 0.75, 1.25, and 1.5 over the Reynolds-number range $Re = 300$–700. The purpose of this sweep is to determine whether increasing the upper-step area improves the thermal performance of the two-step rib without producing an excessive hydraulic penalty.

As shown in Fig. 7(a), increasing A_2/A generally improves the heat-transfer performance of the two-step rib. The configurations with $A_2/A = 1.25$ and $A_2/A = 1.5$ provide higher $\bar{N}u/\bar{N}u_0$ than the smaller upper-step cases. This behavior indicates that enlarging the upper step strengthens the interaction between the flow and the ribbed region. A larger upper step increases the effective obstruction and promotes stronger local disturbance in the transverse microchamber, which can improve thermal-boundary-layer interruption

and fluid mixing. Similar heat-transfer enhancement mechanisms have been reported for ribbed interrupted microchannels, where rectangular ribs induce flow separation, recirculation, and local redevelopment of the thermal boundary layer [17].

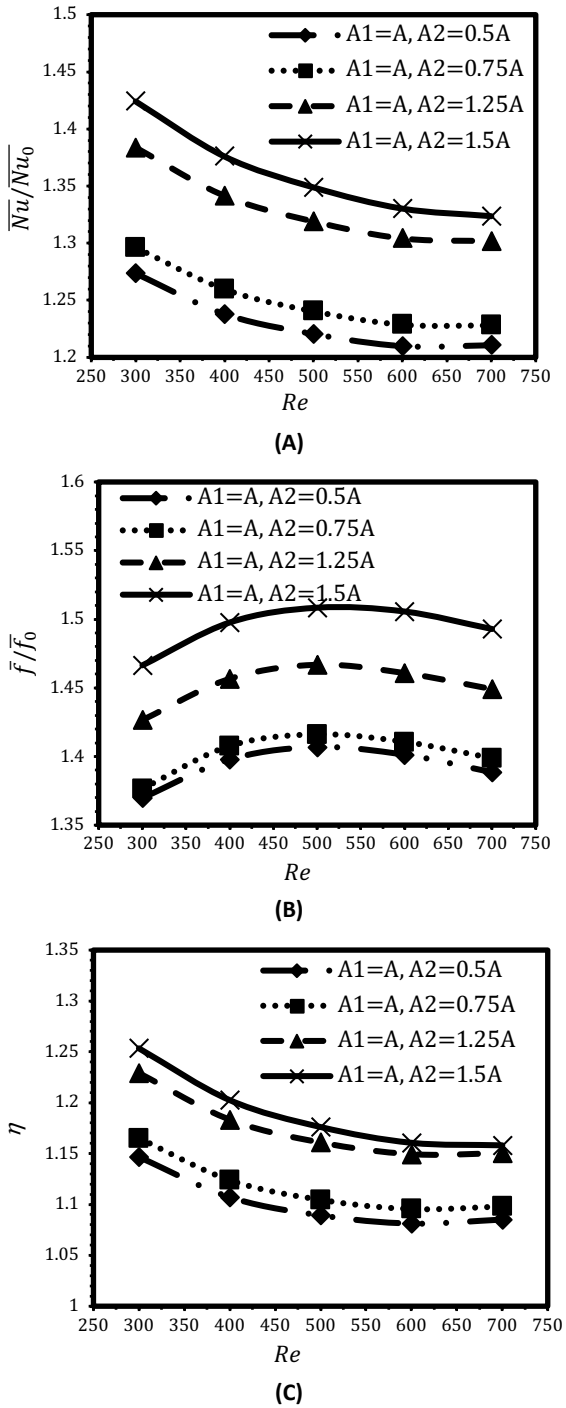


Fig. 7. (A) Variation of $\overline{\boldsymbol{Nu}}/\overline{\boldsymbol{Nu}}_{\boldsymbol{0}}$, (B) variation of $\bar{\boldsymbol{f}}/\bar{\boldsymbol{f}}_{\boldsymbol{0}}$ and (C) variation of η with Re for different areas of two-step ribs.

The hydraulic response is presented in Fig. 7(b). The friction-factor ratio increases as A_2/A becomes larger, showing that the heat-transfer improvement is accompanied by additional flow resistance. This is expected because a larger upper step narrows the available flow passage and increases local contraction,

expansion, and form-drag effects. Therefore, although increasing the upper-step area improves the average Nusselt number, it also increases the pumping-power demand. This confirms that the upper-step area cannot be judged using heat-transfer performance alone; it must be evaluated together with the friction penalty. The combined thermo-hydraulic behavior is shown in Fig. 7(c). The thermal enhancement factor remains greater than unity for all two-step configurations, indicating that each tested design provides a net performance improvement compared with the straight rectangular microchannel at equal pumping power. Among the tested area ratios, $A_2/A = 1.5$ gives the highest η over the investigated Reynolds-number range. The case $A_2/A = 1.25$ also performs well and remains close to the best case, while producing a lower friction-factor ratio. Therefore, $A_2/A = 1.5$ can be considered the best-performing configuration within the tested range, whereas $A_2/A = 1.25$ may be preferred when a lower hydraulic penalty is required.

Table 6. Variation of $\overline{Nu}/\overline{Nu_0}$ with Re for different areas of two-step ribs, using the base rib area A

A2/Re	300	400	500	600	700
0.5A	1.52	1.49	1.57	1.46	1.46
0.75A	1.55	1.51	1.48	1.48	1.48
1.25A	1.63	1.59	1.55	1.55	1.55
1.5A	1.67	1.63	1.60	1.58	1.57

Table 7. Variation of $\overline{f}/\overline{f}_0$ with Re for different areas of two-step ribs, using the base rib area A

A2/Re	300	400	500	600	700
0.5A	1.61	1.65	1.66	1.65	1.64
0.75A	1.63	1.66	1.67	1.66	1.65
1.25A	1.68	1.71	1.71	1.70	1.70
1.5A	1.71	1.75	1.75	1.76	1.74

Quantitatively, the largest upper-step area ratio, $A_2/A = 1.5$, gives the highest heat-transfer ratios at all tested Reynolds numbers, with $\bar{N}u/\bar{N}u_0$ decreasing from 1.67 at $Re = 300$ to 1.57 at $Re = 700$. The $A_2/A = 1.25$ case gives slightly lower heat-transfer ratios, ranging from 1.63 to 1.55 over the same Reynolds-number interval. The corresponding friction-factor ratios also increase with area ratio. For $A_2/A = 1.5$, f/f_0 remains within 1.71–1.76, while for $A_2/A = 1.25$, it remains within 1.68–1.71. Thus, the performance improvement obtained by increasing the upper-step area is not free of hydraulic cost; however, within the present range, the heat-transfer gain is sufficient to maintain a higher thermal enhancement factor for the larger upper-step designs.

4. Conclusions

A three-dimensional numerical investigation was carried out to evaluate the thermo-hydraulic performance of interrupted microchannel heat sinks equipped with multi-step rectangular ribs. The simulations were conducted over $Re = 300–700$, and the model was validated against published interrupted-MCHS data. The maximum deviation in the average Nusselt number was 6.98%, confirming that the present numerical model provides acceptable accuracy for the subsequent parametric analysis. The first parametric sweep examined the effect of rib step number, $N = 2$, 3, and 4. All ribbed configurations improved heat transfer relative to the straight rectangular microchannel baseline. At $Re = 300$, the three-step rib produced the highest heat-transfer ratio, with $\bar{Nu}/\bar{Nu}_0 = 1.52$, compared with 1.49 for $N = 4$ and 1.30 for $N = 2$. However, for $Re \geq 400$, the two-step rib became the best-performing configuration in terms of heat transfer, giving $\bar{Nu}/\bar{Nu}_0 = 1.54$, 1.52, 1.51, and 1.50 at $Re = 400$, 500, 600, and 700, respectively. The friction-factor ratio of the two-step case remained within $f/f_0 = 1.57–1.61$, which was only slightly higher than those of the three-step and four-step cases. As a result, the two-step rib provided the most favorable overall thermo-hydraulic performance for moderate-to-high Reynolds numbers. The second parametric sweep focused on the two-step rib and examined the effect of upper-step area ratio, A_2/A. Increasing A_2/A improved heat-transfer performance but also increased hydraulic resistance. The largest tested area ratio, $A_2/A = 1.5$, produced the highest heat-transfer ratios, with $\bar{Nu}/\bar{Nu}_0$ decreasing from 1.67 at $Re = 300$ to 1.57 at $Re = 700$. This corresponds to a heat-transfer enhancement of approximately $57–67\%$ compared with the straight baseline channel. The corresponding friction-factor ratio remained within $f/f_0 = 1.71–1.76$, indicating a pressure-loss penalty of approximately $71–76\%$. Despite this increase in flow resistance, the thermal enhancement factor remained the highest among the tested two-step designs, ranging from $\eta = 1.397$ at $Re = 300$ to $\eta = 1.305$ at $Re = 700$. The case $A_2/A = 1.25$ also showed strong performance, with $\bar{Nu}/\bar{Nu}_0 = 1.55–1.63$, $f/f_0 = 1.68–1.71$, and $\eta = 1.296–1.371$. Therefore, $A_2/A = 1.5$ is recommended when maximum thermal enhancement is the main objective, while $A_2/A = 1.25$ provides a near-optimal alternative when a lower hydraulic penalty is preferred. Overall, the results demonstrate that increasing rib complexity alone does not guarantee better performance. The best configuration is obtained by balancing heat-transfer enhancement with frictional losses. Within the investigated range, the optimized two-step rectangular rib, particularly with $A_2/A = 1.5$, provides the strongest overall improvement and offers a practical geometry for enhancing compact liquid-cooled microchannel heat sinks used in high-performance electronic cooling applications.

Nomenclature

Symbol	Description	Unit
A	Base rib area	m²
A_2	Upper-step rib area	m²
c_p	Specific heat of fluid at constant pressure	J kg^{-1} K^{-1}
D	Hydraulic diameter of microchannel	m
f	Fanning friction factor	–
h	Local convective heat-transfer coefficient	W m^{-2} K^{-1}
k_f	Thermal conductivity of fluid	W m^{-1} K^{-1}
k_s	Thermal conductivity of solid substrate	W m^{-1} K^{-1}
L	Heated length of channel	m
N	Number of rib steps per microchamber	–
Nu	Local or average Nusselt number	–
$\bar{Nu}$	Mean Nusselt number along heated length	–
Δp	Pressure drop across heated length	Pa
q''	Applied uniform heat flux	W m^{-2}
Re	Reynolds number ($\rho u_m D/\mu$)	–
T	Temperature	K
T_b	Bulk (mass-flow averaged) temperature	K
T_w	Wall temperature	K
u, v, w	Velocity components in x, y, z directions	m s^{-1}
u_m	Mean velocity at channel inlet	m s^{-1}
x, y, z	Cartesian coordinates	m
ρ	Fluid density	kg m^{-3}
μ	Dynamic viscosity	Pa s
η	Thermal enhancement (performance evaluation) factor	–
Φ	Viscous dissipation term in energy equation	W m^{-3}

Subscripts and superscripts

Symbol	Meaning
f	Fluid
s	Solid substrate
0	Baseline (straight rectangular microchannel)
in	Inlet
out	Outlet

Abbreviations

Abbreviation	Definition
CFD	Computational Fluid Dynamics
MCHS	Microchannel Heat Sink
IMCHS	Interrupted Microchannel Heat Sink
PEC	Performance Evaluation Criterion
Re	Reynolds Number
Nu	Nusselt Number
VOF	Volume of Fluid
HPC	High-Performance Computing
CPU	Central Processing Unit
GPU	Graphics Processing Unit

References

[1] International Roadmap for Devices and Systems. (2024). *International roadmap for devices and systems: 2024 edition*. IEEE. https://irds.ieee.org

[2] Tuckerman, D. B., & Pease, R. F. W. (1981). High-performance heat sinking for VLSI. *IEEE Electron Device Letters, 2*(5), 126–129. https://doi.org/10.1109/EDL.1981.25367

[3] Sobhan, C. B., & Garimella, S. V. (2001). A comparative analysis of studies on heat transfer and fluid flow in microchannels. *Microscale Thermophysical Engineering, 5*(4), 293–311. https://doi.org/10.1080/10893950152646759

[4] Xu, J. L., Gan, Y. H., & Zhang, D. C. (2005). Microscale heat transfer enhancement using thermal boundary layer redeveloping concept. *International Journal of Heat and Mass Transfer, 48*(9), 1662–1674. https://doi.org/10.1016/j.ijheatmasstransfer.2004.10.021

[5] Xu, J. L., Song, Y. X., & Zhang, W. (2008). Numerical simulations of interrupted and conventional microchannel heat sinks. *International Journal of Heat and Mass Transfer, 51*(23–24), 5906–5917. https://doi.org/10.1016/j.ijheatmasstransfer.2008.03.033

[6] Cheng, Y. J. (2007). Numerical simulation of stacked microchannel heat sink with mixing-enhanced passive structure. *International Communications in Heat and Mass Transfer, 34*(3), 295–303. https://doi.org/10.1016/j.icheatmasstransfer.2006.12.007

[7] Hong, F., & Cheng, P. (2009). Three dimensional numerical analyses and optimization of offset strip-fin microchannel heat sinks. *International Communications in Heat and Mass Transfer, 36*(7), 651–656. https://doi.org/10.1016/j.icheatmasstransfer.2009.02.015

[8] Foong, A. J., Ramesh, N., & Chandratilleke, T. T. (2009). Laminar convective heat transfer in a microchannel with internal longitudinal fins. *International Journal of Thermal Sciences, 48*(10), 1908–1913. https://doi.org/10.1016/j.ijthermalsci.2009.02.015

[9] Chai, L., Xia, G. D., & Zhou, M. Z. (2011). Numerical simulation of fluid flow and heat transfer in a microchannel heat sink with offset fan-shaped reentrant cavities in sidewall. *International Communications in Heat and Mass Transfer, 38*(5), 577–584. https://doi.org/10.1016/j.icheatmasstransfer.2010.12.037

[10] Xia, G. D., Chai, L., & Zhou, M. Z. (2011). Effects of structural parameters on fluid flow and heat transfer in a microchannel with aligned fan-shaped reentrant cavities. *International Journal of Thermal Sciences, 50*(3), 411–419. https://doi.org/10.1016/j.ijthermalsci.2010.08.009

[11] Xia, G. D., Chai, L., & Wang, H. Y. (2011). Optimum thermal design of microchannel heat sink with triangular reentrant cavities. *Applied Thermal Engineering, 31*(6–7), 1208–1219. https://doi.org/10.1016/j.applthermaleng.2010.12.004

[12] Chai, L., Xia, G. D., Wang, L., Zhou, M. Z., & Cui, Z. Z. (2013). Heat transfer enhancement in microchannel heat sinks with periodic expansion–constriction cross-sections. *International Journal of Heat and Mass Transfer, 62*, 741–751. https://doi.org/10.1016/j.ijheatmasstransfer.2013.03.045

[13] Xia, G. D., Zhai, Y. L., & Cui, Z. Z. (2013). Numerical investigation of thermal enhancement in a micro heat sink with fan-shaped reentrant cavities and internal ribs. *Applied Thermal Engineering, 58*(1–2), 52–60. https://doi.org/10.1016/j.applthermaleng.2013.04.005

[14] Xia, G., Zhai, Y., & Cui, Z. (2013). Characteristics of entropy generation and heat transfer in a microchannel with fan-shaped reentrant cavities and internal ribs. *Science China Technological Sciences, 56*(7), 1629–1635. https://doi.org/10.1007/s11431-013-5244-z

[15] Ghani, I. A., Kamaruzaman, N., & Sidik, N. A. C. (2017). Heat transfer augmentation in a microchannel heat sink with sinusoidal cavities and rectangular ribs. *International Journal of Heat and Mass Transfer, 108*, 1969–1981. https://doi.org/10.1016/j.ijheatmasstransfer.2017.01.046

[16] Chai, L., & Wang, L. (2018). Thermal-hydraulic performance of interrupted microchannel heat sinks with different rib geometries in transverse microchambers. *International Journal of Thermal Sciences, 127*, 201–212. https://doi.org/10.1016/j.ijthermalsci.2018.01.029

[17] Chai, L., Xia, G. D., Zhou, M. Z., Li, J., & Qi, J. Z. (2013). Optimum thermal design of interrupted microchannel heat sink with rectangular ribs in the transverse microchambers. *Applied Thermal Engineering, 51*(1–2), 880–889. https://doi.org/10.1016/j.applthermaleng.2012.10.037

[18] Bird, R. B., Stewart, W. E., & Lightfoot, E. N. (2002). *Transport phenomena* (2nd ed.). John Wiley & Sons.

[19] Patankar, S. V. (1980). *Numerical heat transfer and fluid flow*. Hemisphere Publishing.

[20] White, F. M. (2006). *Viscous fluid flow* (3rd ed.). McGraw-Hill.

[21] Incropera, F. P., DeWitt, D. P., Bergman, T. L., & Lavine, A. S. (2011). *Fundamentals of heat and mass transfer* (7th ed.). John Wiley & Sons.

[22] Versteeg, H. K., & Malalasekera, W. (2007). *An introduction to computational fluid dynamics: The finite volume method* (2nd ed.). Pearson Education.

[23] Kays, W. M., Crawford, M. E., & Weigand, B. (2005). *Convective heat and mass transfer* (4th ed.). McGraw-Hill.

[24] Shah, R. K., & London, A. L. (1978). *Laminar flow forced convection in ducts*. Academic Press.

[25] Webb, R. L., & Eckert, E. R. G. (1971). Heat transfer and friction in tubes with repeated-rib roughness. *International Journal of Heat and Mass Transfer, 14*(4), 601–617. https://doi.org/10.1016/0017-9310(71)90189-5

[26] Manglik, R. M., & Bergles, A. E. (1993). Heat transfer and pressure drop correlations for twisted-tape inserts in isothermal tubes: Part II—Transition and turbulent flows. *Journal of Heat Transfer, 115*(4), 890–896.

[27] ANSYS, Inc. (2007). *ANSYS Fluent 6.3 user's guide*. ANSYS, Inc.

[28] Roache, P. J. (1998). *Verification and validation in computational science and engineering*. Hermosa Publishers.

[29] Oberkampf, W. L., & Trucano, T. G. (2002). Verification and validation in computational fluid dynamics. *Progress in Aerospace Sciences, 38*(3), 209–272. https://doi.org/10.1016/S0376-0421(02)00005-2